X-ray generation in a cavity heated by 1.3- or 0.44-μm laser light. II. Time-resolved measurements

G. D. Tsakiris and R. Sigel
Max-Planck-Institut für Quantenoptik, D-8046 Garching, Federal Republic of Germany
(Received 17 May 1988)

Results are presented from experiments aiming at the study of the process of thermalization and confinement of the laser energy in closed geometry targets. The interior of spherical gold cavities (0.3–1.0 mm in diameter) has been irradiated with 300-ps pulses at average laser fluxes between 2×10^{12} and 5×10^{13} W/cm^2. A systematic study has been performed at 1.3- and 0.44-μm laser wavelength. The time-resolved x-ray spectrum of the radiation emitted by the cavities shows a double pulse structure. Furthermore, for $\lambda=1.3$ μm and during the second emission burst, M-band emission is observed. Analysis supports the hypothesis that, while the first burst emanates from the indirectly heated wall element, the second burst is due to expanding coronal plasma. Measurements showed that more favorable conditions can be achieved for $\lambda=0.44$ μm and deleterious effects like plasma filling and entrance hole closure can be avoided.

I. INTRODUCTION

In the concept of generation of intense Planck radiation in a small cavity of high-Z material using pulsed laser light,[1] a two-step process is involved. In the first step, the laser energy is partially converted into x-ray radiation, and in the second step, the x rays are thermalized and confined through multiple absorption and reemission. The analysis of recent experiments has shown[2] that the effectiveness of the overall process may depend strongly on the physical processes occurring in the first step, i.e., on the phenomena associated with the laser generated plasma. Since the objective of our studies is the optimization of the mechanism that leads to the thermalization of the laser energy, it becomes necessary that the phenomena associated with the first step be studied and their role in the overall process ascertained. The work reported in this paper is along this line and it is a part of systematic investigations performed on spherical cavities using the Asterix III iodine laser facility.

The method employed to heat cavities with a single laser beam is schematically shown in Fig. 1. The laser beam is focused at the plane of the entrance hole of a spherical cavity with a diameter of a fraction of a millimeter. At the rear wall of the cavity, the "primary plasma" is produced having properties similar to those of the laser-produced plasma with planar targets. Since the cavity wall is made out of high-Z material, a relatively large fraction of the laser energy is converted to x rays. The primary plasma acts approximately as a Lambert emitter of x-ray radiation and due to the spherical geometry, uniformly illuminates the interior of the cavity. As a consequence, a "secondary plasma" is produced with properties quite different than those of the primary plasma; it is colder and denser. Owing to the combination of temperature and density, the secondary plasma layer is opaque to x-ray photons existing in the interior of the cavity. It acts as a reflecting layer preventing the photons from penetrating deeply into the cavity wall. The secondary plasma layer is a "reflector" but not in the usual sense; a photon is absorbed and reemitted. The process of multiple absorption and reemission is the underlying mechanism that leads to thermalization and confinement of the radiation inside the cavity.

The scaling relations derived from the self-similar solution to the radiation hydrodynamic equations for the secondary plasma[3] indicate that the temperature in the cavity and the number of reemissions N increase with incident energy flux and pulse duration. For a given incident x-ray flux, the number N of absorptions and reemissions of a photon (corresponding to the quality factor of the cavity for the confinement of thermal radiation) de-

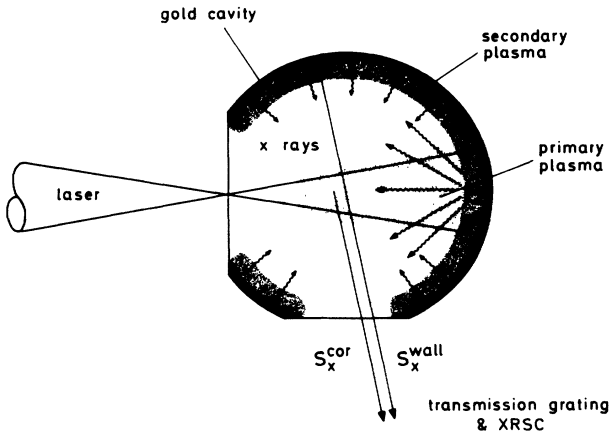

FIG. 1. Schematic drawing of the method used to heat cavities. In addition to the entrance hole through which the laser is coupled to the cavity, a diagnostic hole is used for probing the x-ray radiation generated in the cavity. The arrows indicate the line of sight of the x-ray streak camera (XRSC) which detects radiation from the secondary plasma (x-ray ablated plasma), but also from the corona of the primary plasma (laser ablated plasma).

pends on the balance between the heating of the material by the incident flux of primary x rays and the loss of energy by diffusion of radiation into the deeper lying part of the wall which, ultimately, is converted into hydrodynamic motion of the expanding secondary plasma layer. As in the case of a microwave cavity, where the conductivity of the wall material determines the quality factor, it is the opacity of the wall material and its functional dependence on density and temperature that determines the quality factor of an x-ray confining cavity.[3,4] Since high-Z materials exhibit the highest opacity values,[5] they are preferentially employed in fabricating cavities.

In the present investigations, we have attempted to obtain time-resolved experimental information about the process of cavity heating with the help of an x-ray streak camera. The streak camera was combined with a transmission grating in order to obtain time-resolved spectra. Ideally, i.e., if the cavity would remain empty during heating, the radiation registered through a diagnostic hole in the cavity (see Fig. 1) would come only from the secondary plasma on the x-ray heated wall. In this case, the situation would correspond closely to the idealized model[3] of cavity heating and the results could readily be compared with the theoretical predictions. However, as suggested already by the way Fig. 1 has been drawn, the situation may be more complicated due to expansion of the primary plasma into the cavity and simultaneously into the line of sight of the x-ray streak camera. The identification of the contribution of the expanding primary plasma to the measured spectra is a major point of the present investigation.

The complication introduced by the expanding primary plasma is a consequence of incomplete x-ray conversion in the primary plasma. The unconverted part of the absorbed laser energy appears as internal and kinetic energy of the expanding plasma. Therefore, the lower the conversion efficiency into x rays, the more severe the problem is. Experiments with planar targets have shown that the conversion efficiency is higher the shorter the wavelength of the laser light, with a tendency to decrease at higher laser fluxes.[6–16] More specifically, the x-ray conversion efficiency for laser fluxes between 10^{14} and 10^{15} W/cm^2 and for pulse duration of 300 ps was found to be 10–20% for 1.3-μm and 40–60% for 0.44-μm laser light.[17] It is obvious that the single-beam irradiation is not ideal in this respect because it has the consequence of a very high local laser flux. Furthermore, the laser wavelength is expected to play a major role, not only because the conversion efficiency decreases with increasing laser wavelength, but also because the temperature of the primary plasma and, hence, the expansion velocity is expected to increase with the laser wavelength. A cavity heated by long wavelength laser light will, therefore, fill faster than one heated by short-wavelength laser light.

In these investigations, we have varied the wavelength of the laser light and performed comparative measurements at the fundamental ($\lambda=1.3$ μm) and triple ($\lambda=0.44$ μm) frequency of the laser light. The results of our studies are reported in three companion papers (papers I, II, and III). This is paper II and concerns itself primarily with the results of the time-resolved x-ray spectroscopy and their interpretation. The experimental results and discussion of the time-integrated measurements are presented in the companion paper,[18] paper I. Finally, paper III (Ref. 19) deals with the comparison of the experimental results from the time-integrated measurements with theoretical predictions for radiation confinement in the cavity.[3] It should be mentioned here that, although each one of the three papers dealing with the results of these comprehensive studies has been written as an independent and self-contained report, a more complete picture can be obtained by reading all three parts.

II. EXPERIMENTAL ARRANGEMENT

A. Parameter range of the experiments

For the cavity target experiments the single-beam Asterix III laser facility was used; it produces routinely 80 J at $\lambda=1.3$ μm (1ω) and 20 J at $\lambda=0.44$ μm (3ω) in 300 ps. The cavities are made out of 2-μm-thick gold and typically have two holes; one is used to inject the laser energy into the cavity and the other as an observation port (see Fig. 1). The laser energy is introduced into the cavity by focusing it with an aspheric lens of an effective f number 2.5. In the present experiments, the cavity diameter was varied between 250 and 1000 μm. The laser entrance hole and diagnostic hole diameter were scaled proportionally to the cavity diameter and were in the ranges 145–530 and 98–234 μm, respectively. An array of diagnostics was simultaneously deployed in these experiments to characterize the heating process of the cavity. The emphasis was on soft-x-ray diagnostics which included x-ray pinhole photography and time-integrated and time-resolved x-ray spectroscopy. In addition, optical shadowgraphy was used and the laser absorption was measured using a light integrating box.[20] A more detailed description of the experimental setup and a discussion of the results from the rest of the diagnostics is given in the first companion paper (paper I).

B. Time-resolving soft-x-ray spectrometer

The time-resolved soft-x-ray spectra were obtained using a free-standing transmission grating spectrometer coupled to a soft x-ray streak camera.[21] The grating is integrated on a 50-μm-wide and 1-mm-high slit and it has 1000 line pairs/mm. The spectrum is dispersed along the slit of the x-ray streak camera photocathode which is 18 mm long and 300 μm wide. The photocathode is of the transmission type and it consists of 1000-Å-thick carbon substrate on which 1100 Å CsI is deposited. The spectral range covered is between 5 and 100 Å with a time resolution of about 15 ps and spectral resolution of few Å (typically 3–7 Å depending on the size of the diagnostic hole). The short-wavelength limit (≈ 5 Å) of the spectral range is due to overlapping between the zeroth and first order of the spectrum (for $\lambda < 5$ Å the zeroth-order contribution dominates). The streaked spectra are recorded on negative film and subsequently converted to digital form

with the help of a two-dimensional (2D) microdensitometer. Computer processing is employed to analyze the x-ray streak camera records with special softwave developed for this purpose. The data-reduction procedure is performed in three steps. In the first step, an appropriate subframe is selected from the original frame for further processing. In the second step, the selected subframe is linearized using the density curve of the film and corrected for distortions due to the image intensifier. In the final step, the spectrum is deconvolved using the grating efficiency and combined spectral sensitivity of the photocathode and carbon substrate. In order to obtain an absolute value of the spectral intensity as function of time, the deconvolved streaked spectra are numerically integrated over time and compared to the time-integrated spectra recorded on absolutely calibrated Kodak 101 x-ray film.[22] By means of this comparison, the calibration factor for the overall efficiency of the streak camera is determined. The spectrometer was located in the horizontal plane and its viewing direction was slightly larger than 90° with respect to the laser axis. This way, the x-ray streak camera records radiation emanating from the interior wall of the cavity lying opposite to the diagnostic hole through which the radiation is detected. The arrangement is shown schematically in Fig. 1.

An example of a time-resolved spectrum produced by a laser-heated cavity is shown in Fig. 2. The raw data (on film) are shown in Fig. 2(a). Figure 2(b) shows the same data in digitized form (isodensity plots in linear scale). A subframe depicting the details of the zeroth-order structure is shown in Fig. 2(c), while another subframe which is used for further processing and deconvolution of the spectrum during the heating phase is shown in Fig. 2(d). It is interesting to note the splitting of the zeroth order into three discrete lines. The grating slit acts as a one-dimensional imaging system and the zeroth order represents the one-dimensional image of any source present. The diagnostic hole gives rise to the main zeroth order in the middle and to the associated spectrum in the first orders. To the left and right of the main x-ray source, however, there exist two weaker sources; one is due to plasma streaming out of the entrance hole of the cavity and possibly to plasma created at the rim of the entrance hole, and the other is due to emission from the rear wall of the cavity where the primary plasma is located. The curvature of the first order is an artifact and has its origin in the pin-cushion distortion of the image intensifier which is attached to the image converter tube of the streak camera. In the second step of the data reduction, this effect is removed using an appropriate mapping transformation which describes the imaging distortion present in the intensifier.[23]

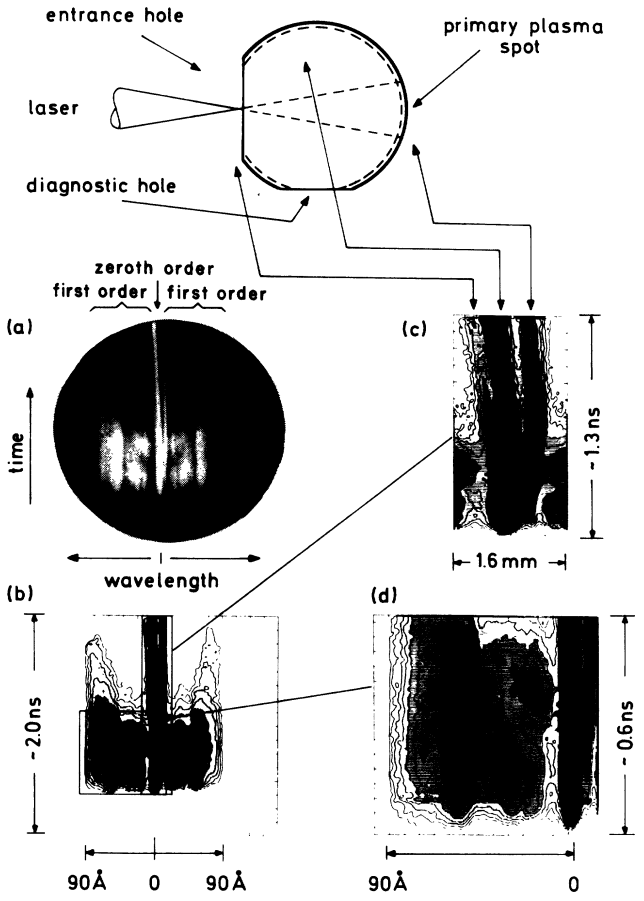

FIG. 2. Time-resolved spectrum from a cavity (laser wavelength 0.44 μm, cavity diameter 467 μm) obtained with a free-standing transmission grating and an x-ray streak camera: (a) raw data on film, (b) digitized record, (c) subframe showing the detailed structure of the zeroth order and its relation to the various emission regions of the cavity (schematic at the top), and (d) subframe used for further processing to obtain the deconvolved cavity spectrum shown in Fig. 3(b).

III. TEMPORALLY RESOLVED CAVITY SPECTRA

A. Structure of the zeroth order

Although the main information delivered by the x-ray streak camera is the time-resolved spectrum associated with the emission from the diagnostic hole (the spectra from the other two sources are at least one order of magnitude less intense and do not interfere with the main spectrum), there is still information to be gained by closely examining the structure of the zeroth order. As can be seen from Figs. 2(a) and 2(c), the zeroth orders due to diagnostic hole and entrance hole run parallel to each other in time indicating that, for the laser-pulse duration, the distance between the two sources does not change appreciably. The zeroth order generated by the entrance hole peaks right at the beginning of the emission. In contrast, the zeroth order due to the primary plasma spot peaks at $\sim$250 ps later. Furthermore, the source associated with this zeroth order is clearly not stationary; it appears to accelerate at the beginning until it reaches its maximum emission and subsequently moves with constant velocity. The simplest explanation for this is that the part of the wall where the primary plasma spot is formed is preferentially accelerated due to higher laser flux there and eventually is pushed out. Because the wall thickness decreases due to lateral expansion as it is pushed into the

direction of the laser beam, emission from the primary plasma spot can penetrate through the thinned out part of the wall, causing a delayed maximum in the emission. Another possible explanation is that the peak emission coincides with the arrival of the ablative heat wave[3] which propagates ahead of the ablation front. We note that the preferential acceleration of the laser-irradiated part of the rear wall has been clearly observed by high-speed photography (see paper I). Also the time-integrated x-ray pinhole photography presented in paper I clearly show the existence of emission areas at the entrance hole and rear wall (see Fig. 3 in paper I). In general, the time-integrated results correlate very well with the observations just described.

B. Time history of the spectrum

We now turn our attention to the spectrum of the radiation emitted by the cavity through the diagnostic hole. The time history of such a spectrum can be divided into two phases; the heating phase and the cooling phase. The heating phase takes place during laser irradiation and it lasts ~ 600 ps; this corresponds to the duration of the emission from planar target with the same laser pulse duration of FWHM 300 ps. The second phase is the cooling phase and its duration depends on the cavity size and laser flux. The two phases are indicated in Fig. 2(b); the heating phase is the subframe shown also in Fig. 2(d) while the cooling phase is the relatively soft (70–90 Å) emission occurring afterwards. The emission during the cavity cooldown has been observed before[4,24] and it has been attributed to the stagnation of the expanding plasma near the center of the cavity. At this later time, part of the kinetic energy of the expanding plasma is converted into thermal energy by collisions which causes a prolongation of the emission. We should emphasize here that our discussion is confined to the heating phase, i.e., during the time that the laser pulse is on, and that from each cavity spectrum a similar subframe, such as the one in Fig. 2(d), is selected which is further processed to obtain the deconvolved spectra shown in Figs. 3, 4, and 5.

It is apparent that the cavity diameter D represents another important parameter; in these experiments the smallest cavity is 250 μm in diameter and the largest is 1 mm. The cavities can be classified according to their size as intermediate size cavities for 400 μm $< D <$ 600 μm, small cavities for $D <$ 400 μm and large for $D >$ 600 μm. This classification is based on the fact that, for each size range, the time-resolved spectrum is different. As will be discussed in detail later on, characteristic for the intermediate size cavities is the appearance of the double-pulse structure in the time-resolved spectra during the heating phase. Because this effect is the key observation for the understanding of the phenomena occurring inside the cavity, we shall concentrate in the following first on the results from the intermediate size cavities.

In Figs. 3 and 4, two sets of deconvolved streaked spectra produced by cavities of increasing size and for two wavelengths are shown. The effect of increasing the cavity diameter for $\lambda = 0.44$ μm (3ω) is depicted in Fig. 3. In all spectra, one can distinguish two emission bursts separated by a time interval Δt, which increases with the

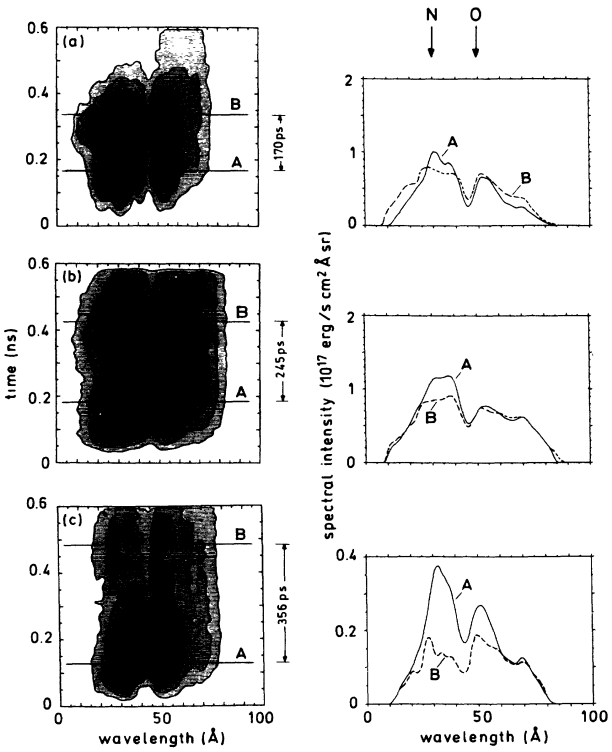

FIG. 3. Deconvolved streaked spectra from cavities irradiated with $\lambda = 0.44$-μm laser light for different cavity diameters [(a) 405 μm, (b) 467 μm, and (c) 555 μm]. The instantaneous spectra corresponding to the peak emission during the first (A) and second (B) burst are shown to the right. For each diameter, the delay Δt representing the approximate time interval between first and second burst is given.

cavity diameter. Furthermore, the spectrum in the second burst appears to be slightly harder than the one in the first [see Fig. 3(a)], but it becomes softer and weaker as the diameter increases.

The deconvolved streaked spectra for approximately the same size cavities but for $\lambda = 1.3$ μm (1ω) are shown in Fig. 4. In this case we observe again two distinct emission bursts but no significant variation with the diameter in the time interval between the two bursts. Although the laser energy available in the fundamental frequency is approximately a factor of 3 to 4 higher than when upconverted to 3ω, the spectra in the first burst in Fig. 4 are not noticeably harder than those in Fig. 3. This can be attributed to two effects that partially compensate for the higher energy. Namely, for $\lambda = 1.3$ μm, the x-ray conversion efficiency at the primary spot and the amount of energy absorbed in a cavity of a given diameter are lower.[13,17,20] However, as seen from Figs. 3 and 4, the difference in the spectra of the second burst is striking. During the second burst, for $\lambda = 1.3$ μm, there is considerable emission at 5 Å (~ 2 keV) which represents M-band emission of gold. Note that this feature is entirely absent from the spectra with $\lambda = 0.44$ μm. In the same time-resolved spectra, the N and O band of the gold spec-

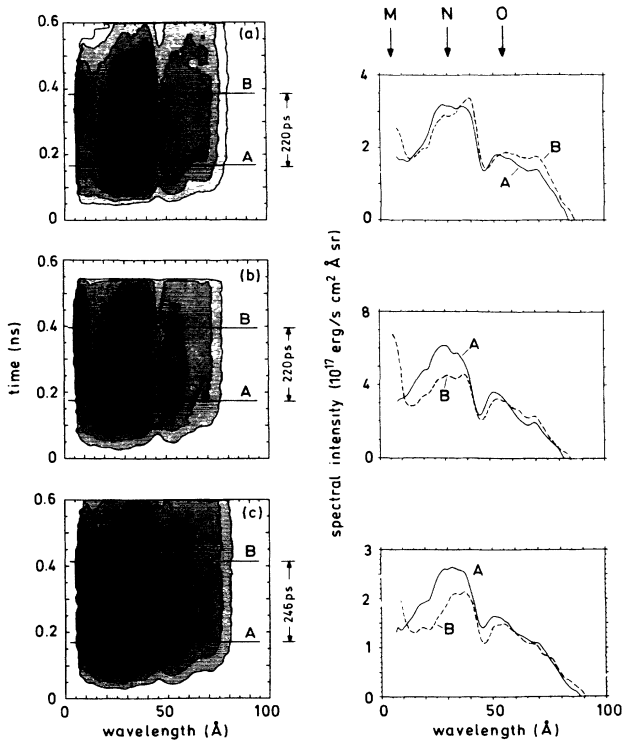

FIG. 4. Deconvolved streaked spectra from cavities irradiated with $\lambda=1.3$-μm laser light for different cavity diameters [(a) 406 μm, (b) 456 μm, and (c) 519 μm]. The instantaneous spectra corresponding to the peak emission during the first (A) and second (B) burst are shown to the right. For each diameter, the delay Δt representing the approximate time interval between first and second burst is given. Note the appearance of the M-band emission during the second burst.

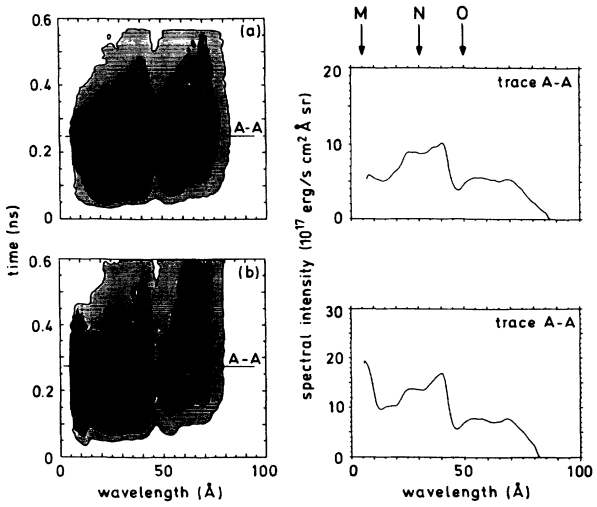

FIG. 5. Deconvolved streaked spectra produced by small cavities ($D=252$ μm) for (a) $\lambda=0.44$-μm and (b) $\lambda=1.3$-μm irradiation. The instantaneous spectrum corresponding approximately to peak emission (trace A-A) for the two cases is also shown.

trum are seen as part of the emission in the first burst.

When the size of the cavity is further reduced ($D<400$ μm, small cavities), the two emission bursts tend to merge together and for the smallest diameter cavities ($D=252$ μm) there is no apparent temporal structure in the spectra other than the heating and cooling phase. This is seen in Fig. 5 where the streaked spectra from the smallest cavity for the two wavelengths are shown. It is interesting to note that for the smallest size cavities, M-band emission appears even when $\lambda=0.44$ μm but simultaneously with N and O band [see Figs. 5(a) and 5(b)]. For $\lambda=1.3$ μm, the emission in the M band is higher and sets in early during the heating phase although it peaks again after the N-band emission.

The large cavities ($D>600$ μm) represent the least complicated case since the radius is large enough that there is no interference from the expanding corona. However, the average laser flux is low and, as a consequence, the interior wall remains relatively cold giving rise to low reemission.[25]

IV. DISCUSSION OF THE RESULTS

A. General remarks, the model

Most of the features in the temporal evolution of the x-ray spectrum emitted by cavities can be attributed to the presence of the primary plasma and the associated subcritical plasma blow off termed corona. In particular, in connection with the double-pulse structure, a consistent picture emerges if one assumes that the first emission burst is due to the secondary plasma and the second burst to the expanding coronal plasma. In this section, we summarize the arguments that lead to this picture.

The closed geometry target provides the possibility of isolating the indirectly irradiated wall element and studying the secondary plasma. For example, the arrangement illustrated in Fig. 1 was judiciously chosen so that the x-ray streak camera looks at the secondary plasma while at the same time, the much more intense primary plasma is obstructed by the rear part of the spherical shell. An examination of the time-integrated x-ray image of the cavity viewed from the top justifies this choice of the viewing angle (see paper I, Fig. 3).

Since the primary x-ray photons propagate inside the cavity with the speed of light, the emission from the indirectly heated wall element (secondary plasma) should commence almost simultaneously with the laser pulse. Presumably, for the duration of the first burst, this is the only emission that the streak camera is detecting. However, since the primary plasma suffers expansion, it is inevitable that a part of the plasma blow off will be crossing the line of sight of the streak camera and will enter its field of view. It is, therefore, conceivable that at some time, the underdense plasma in the corona will interfere with the observation of the indirectly heated wall element. Then, the radiation emitted by the corona gives rise to the second burst. Since the corona usually has a temperature of several keV and is optically thin, it can only emit during the laser pulse; right after the end of laser pulse it cools off very rapidly.

We note that the experimental data from intermediate

size cavities (Figs. 3 and 4) show some characteristics that support the hypothesis that the corona from the primary plasma crosses the line of sight of the streak camera.

(a) Later arrival of the second burst for larger cavity diameter (Fig. 3) is to be expected since the distance between the diagnostic hole and the directly heated primary plasma spot becomes greater. The density of the blow-off plasma at a distance of about a cavity radius from the spot has to be high enough to emit at a detectable level. This would occur after some time, when enough mass has been transported through expansion to the point where the line of sight of the streak camera crosses the plasma blow off.

(b) The tendency of the spectrum in the second burst in Fig. 3 to be softer and weaker for larger diameter cavities can be explained as due to lower laser fluxes at the primary plasma spot. The coronal temperature, which determines the spectrum emitted, depends on the irradiation flux. Since for larger cavities the spot size is larger, for the same laser energy the flux would be lower and therefore, the spectrum softer.

(c) The harder radiation observed for $\lambda=1.3$ μm (Fig. 4) is consistent with the assumption that it originates in the corona since for longer laser wavelengths the coronal temperature is higher.

In Secs. IV B and C, the analysis of these experimental observations is presented in a more quantiative fashion.

B. Delay in the appearance of the second burst

The laser flux at the primary plasma spot S_L^{spot} is normally one to two orders of magnitude higher than the flux which produces the secondary plasma [the latter being roughly equal to $\eta_x S_L^{\text{av}}$ where η_x is the x-ray conversion efficiency and $S_L^{\text{av}}=E_L/(\tau_L \pi D^2)$ the average over the inner surface of the cavity laser flux]. Consequently, the x-ray emission from the primary plasma is considerably more intense than the emission from the secondary plasma. This has been confirmed experimentally by viewing the two sources directly and measuring their time-integrated spectrum (see paper I, Figs. 5 and 6). However, the x-ray streak camera does not look directly at the primary plasma, but at some distance x from it approximately equal to the cavity radius R and in a direction almost perpendicular to the density gradient (see Fig. 1), hence, the emission from the low-density blow off is drastically reduced. Indeed, from the data in Figs. 3 and 4 is seen that the emission level in the two bursts is approximately of the same order of magnitude. This means that, in the viewing direction of the x-ray streak camera, the surface emission from the inner cavity wall S_x^{wall} is at the same level with the uniform volume emission S_x^{cor} of the coronal plasma at a distance $x \approx R$ from the primary spot.

Accurate calculation of S_x^{cor} is difficult to perform since the hydrodynamic motion of the expanding plasma in a rather complicated geometry has to be taken into account. In what follows, we present some order of magnitude estimates of the emission from the plasma blow off using a simplified model. We assume isothermal expansion for the primary plasma corona which gives the following dependence of the density on time and coordinate:

$$n_e(x,t)=n_{ec}e^{-x/c_s t}, \tag{1}$$

where

$$c_s=\left[\frac{Z_0 kT_e}{m_i}\right]^{1/2} \tag{2}$$

is the sound velocity and Z_0 the ionization state at a temperature T_e. The critical density for a given laser wavelength is taken as initial density. An estimate of the corona temperature is obtained by equating the laser flux to the free streaming limit for the thermal flux

$$S_L^{\text{spot}}=0.65 f\frac{(kT_e)^{3/2}}{m_e^{1/2}}n_{ec}\ . \tag{3}$$

To obtain more realistic values, a flux limiting factor f has been introduced in Eq. (3). For a given laser wavelength and flux at the directly irradiated spot, the corona temperature is calculated from Eq. (3) and the sound velocity from Eq. (2). The volume emission rate $\epsilon(x,t)$ of the optically thin corona at a distance x from the primary spot is obtained by multiplying the corresponding cooling rate W_Z due to radiation by the electron and ion density, i.e.,

$$\epsilon(x,t)=\frac{W_Z n_e^2(x,t)}{Z_0}\ . \tag{4}$$

For coronal equilibrium, the cooling rate W_Z and the ionization state Z_0 for Au ($Z=79$) as function of temperature are taken from Ref. 26. Finally, the radiation flux emitted by the corona along the line of sight of the streak camera S_x^{cor} is the integral along this line. This is true because the corona is optically thin and no absorption takes place. For our estimations, we multiply the volume emission rate ϵ by a characteristic length along the line of sight. The spot diameter at the rear wall of the cavity $D_{\text{spot}} \approx 200$ μm is taken as the characteristic length. The emitted intensity is therefore estimated using the formula

$$S_x^{\text{cor}}=\epsilon D_{\text{spot}}\ . \tag{5}$$

In Table I, the different quantities used in the simplified model are summarized. Two cases are considered corresponding to the experimental data of Figs. 3 and 4. For $\lambda=1.3$ μm, the flux at the primary spot is approximately a factor of 2–3 higher than for $\lambda=0.44$ μm because of higher laser energy.

It is interesting to estimate first the density $n_e(x=R)$ that is needed at the center of the cavity to produce the observed level of corona radiation. The densities for the two wavelengths are given in the second to last column of Table I and have been obtained from Eq. (5) by setting $S_x^{\text{cor}} \approx S_L^{\text{av}}$. This is justified because the absolute time-integrated spectral measurements (see paper I) have shown that the x-ray flux emanating from the interior of the cavity is within a factor of 2–3 equal to the average laser flux with which the cavity is heated. It follows, therefore, that the fluxes S_x^{wall} and S_x^{cor} are also of the

TABLE I. Summary of the intermediate results for the estimates of the emission from the coronal blow-off plasma at a distance equal to a cavity radius from the laser spot. Two cases have been considered corresponding to $\lambda=1.3$-μm and $\lambda=0.44$-μm irradiation, and for $f=0.08$.

	n_{ec} (cm^{-3})	T_e (keV)	Z_0	c_s (cm/s)	$c_s\tau_L$ (μm)	W_Z ($W\,cm^3$)	S_L^{av} (W/cm^2)	$n_e(x=R)$ (cm^{-3})	t (ps)
$\lambda=1.3$ μm $S_L^{spot}=6.0\times10^{14}$ (W/cm^2)	6.63×10^{20}	18.8	67	7.8×10^{7}	234.0	6.0×10^{-26}	1.9×10^{13}	1.03×10^{21}	
$\lambda=0.44$ μm $S_L^{spot}=2.5\times10^{14}$ (W/cm^2)	5.8×10^{21}	2.5	40	2.2×10^{7}	66.0	5.0×10^{-25}	7.9×10^{12}	1.8×10^{20}	313.0

same order of magnitude as S_L^{av}. As can be seen from Table I, the model predicts a density which is subcritical for $\lambda=0.44$ μm, while for $\lambda=1.3$ μm, it predicts that the radiation is produced in a overdense plasma in which the laser light cannot propagate. It is very satisfactory that the interpretation of the x-ray measurements leads to this conclusion because the optical shadowgraphy, the x-ray pinhole photography, and the absorption measurements reported in paper I have already given clear evidence that strong refraction and reflection of the laser light occurs in $\lambda=1.3$-μm experiments (but not in $\lambda=0.44$-μm experiments).

The delayed occurrence of the second burst for intermediate size cavities is predicted by the model. By combining Eqs. (1), (4), and (5) and solving for the time, one obtains the following relation:

$$t=\frac{2R}{c_s}\left[\ln\left[\frac{n_{ec}^2 W_Z D_{spot}}{S_x^{cor} Z_0}\right]\right]^{-1}. \tag{6}$$

It is seen that, in first approximation, the time required for the density at the center of the cavity to build up to the level that will produce a given x-ray flux S_x^{cor} is proportional to cavity radius. This is in qualitative agreement with the variation of the delay Δt observed in the experimental results of Fig. 3. Again, by setting $S_x^{cor}\approx S_L^{av}$ and for a mean radius of 240 μm, one finds in the case of $\lambda=0.44$-μm irradiation $t=313$ ps (see Table I). Taking the experimental uncertainty due to the lack of a time fiducial into account (in Figs. 3 and 4 the delay is somewhat arbitrarily given relative to the first emission peak), such values appear reasonable and compare favorably with the delay Δt in Fig. 3.

The simple coronal blow-off model must fail for $\lambda=1.3$-μm experiments if, as assumed in Eq. (1), the critical density is taken as initial density (we have seen above that the density in the cavity probably exceeds the critical density for $\lambda=1.3$ μm experiments). There is little doubt, however, that plasma filling is an even stronger effect in $\lambda=1.3$-μm experiments; this tendency may be noted from Table I where the corona temperature, the sound velocity, and the density scale length $c_s\tau_L$ are higher for $\lambda=1.3$ μm. It is, in fact, sufficient to assume a slightly enhanced initial density to make the model applicable to the $\lambda=1.3$-μm experiments. Such an enhancement could occur by energy transport beyond the critical density, for example, by plasma electrons. Due to the low critical density, the $\lambda=1.3$-μm experiments are more sensitive to such an effect. However, it is also possible that other effects, not taken into account in this simple model, play a role in the rapid plasma filling in $\lambda=1.3$-μm experiments. Enhanced mass influx into the cavity in the form of primary plasma produced all over the cavity by reflected laser light is a possibility. Even if the reflected laser light cannot propagate in the cavity, high temperatures are still expected in the slightly overdense plasma in the cavity (according to Table I the density in the cavity does not exceed the critical by more than a factor of 2). They are likely to be generated as the energy is transported from near the entrance hole (where the laser light is absorbed) to the interior of the cavity. However, the situation is more complicated and would need more elaborate models than our simple coronal blow-off model.

C. Spectrum of the coronal emission

The spectrum emitted by the primary plasma (corona) is expected to be harder for $\lambda=1.3$ μm than for $\lambda=0.44$ μm because more energy is available in the fundamental frequency, but more importantly, because for longer wavelengths, the corona temperature is higher (see Table I). The effect of the wavelength on the emitted spectrum by the corona can be understood with the help of Fig. 6 where the cooling rate W_Z is plotted as function of the electron temperature for coronal equilibrium.[26] To obtain some spectral information, we have estimated the power emitted in the various bands due to radiative decay following collisional excitation (CE) from the relation[26,27]

$$W_{CE,n}=8\sqrt{\pi}\alpha a_0^2 c E_H P_n\left[\frac{E_H}{kT_e}\right]^{1/2}\exp\left[-\frac{E_n-E_{n+1}}{kT_e}\right]. \tag{7}$$

Apart from the different physical constants (α is the fine-structure constant, a_0 is the Bohr radius, c is the speed of light, and E_H is the ionization energy of hydrogen), P_n represents the occupation number of the atomic level having principal quantum number n and E_n is the corresponding energy. In this calculation, the "average ion" model[5] is invoked and the approximation $P_n\approx\sum_m f_{nm}$, where f_{nm} are the oscillator strength, has been used. Furthermore, as characteristic excitation energy for the band of lines associated with the principal quantum number n we have taken E_n-E_{n+1}. For a given temperature, the occupation numbers P_n for the average ion in the ground state are calculated from the number of the remaining bound electrons $Z_b=Z-Z_0$. The ionization

state is the one corresponding to coronal equilibrium.[26] Subsequently, the energy levels are calculated using the Slater's screening coefficients. In the calculations, in addition to volume emission due to radiative decay following collisional excitation, we have included radiative losses due to bremsstrahlung,[26,27] i.e.,

$$W_{\rm br}=\frac{64}{3}\left[\frac{\pi}{3}\right]^{1/2}(\alpha a_0)^3\omega_H E_H\left[\frac{kT}{E_H}\right]^{1/2}Z_0^2\ , \qquad (8)$$

where $\omega_H\approx E_H/\hbar=2.06\times10^{16}$ s^{-1}. The total cooling rate is obtained from

$$W_Z=\sum_n W_{{\rm CE},n}+W_{\rm br}\ , \qquad (9)$$

and for Au ($Z=79$), it is shown in Fig. 6 along with the individual contributions from the various bands. For comparison, the more accurate calculation of the cooling rate[26] is also shown. It is seen that the agreement with the simple estimates based on Eqs. (7) and (8) is quite acceptable and within a factor of 2 for most of the temperature range except for the very low temperatures. This discrepancy can be understood as due to rather inaccurate excitation energies predicted by the average ion model for the outermost shells.[5] As expected, a temperature increase results in higher ionization and therefore, emission from successively deeper lying shells. In Fig. 6, the coronal temperature for the laser flux range between $10^{14}-10^{15}$ W/cm^2 and for the two wavelengths is shown by the shaded areas. The temperature is obtained from Eq. (3). Generally, the coronal temperature for $\lambda=0.44$ μm is lower than for $\lambda=1.3$ μm because the laser energy for short wavelengths is deposited at higher densities where more mass is involved. As a consequence, the spectrum from the coronal plasma produced by $\lambda=0.44$-μm irradiation consists primarily of N-band emission. On the other hand, when $\lambda=1.3$ μm the main contribution to the emitted spectrum is from M-band lines (~5 Å). This is in accordance with the observed spectral content of the second burst in both cases, i.e., for $\lambda=0.44$ μm (Fig. 3) and for $\lambda=1.3$ μm (Fig. 4), and supports the assumption that the emission in the second burst comes, in part, from the coronal blow off of the primary plasma. The spectrum from the optically thick secondary plasma is more difficult to calculate since it requires the solution of the radiation transport equation. Previous calculations[4] have shown that increase of the laser flux from 2×10^{12} to 3×10^{13} W/cm^2 causes the peak emission to shift from the O band (40–60 Å) to the N band (15–30 Å) and, finally, to the M band (~5 Å) for even higher fluxes. For the average laser fluxes encountered in the intermediate size cavities, the same calculations show that the spectrum consists mainly of N-band and some O-band emission. This is consistent with the observed spectra in the first burst of Figs. 3 and 4.

The observed spectrum in the second burst is a mixture of relatively hard radiation emanating from the optically thin coronal blow off as well as of softer radiation originating from the secondary plasma on the cavity wall along the line of sight of the streak camera. This is depicted in Fig. 7 where the spectral intensity for the indicated wavelengths as function of time is shown. The position of the laser pulse is arbitrary and it has been adjusted so that its peak coincides with the peak of the first

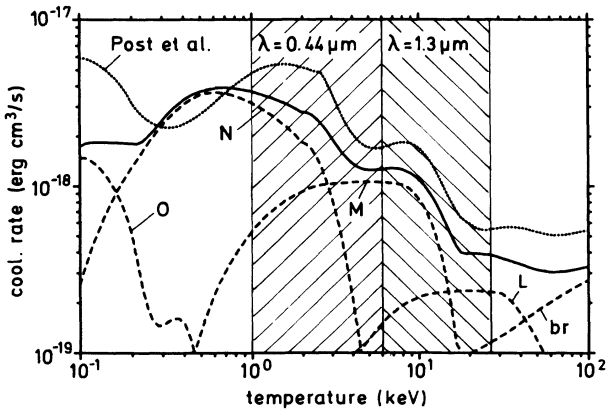

FIG. 6. Steady-state cooling rate of a plasma in coronal equilibrium as function of temperature. The solid line represents the total cooling rate, while the dashed the contributions from the various bands of lines. The dotted line is the cooling rate taken from Post *et al.*

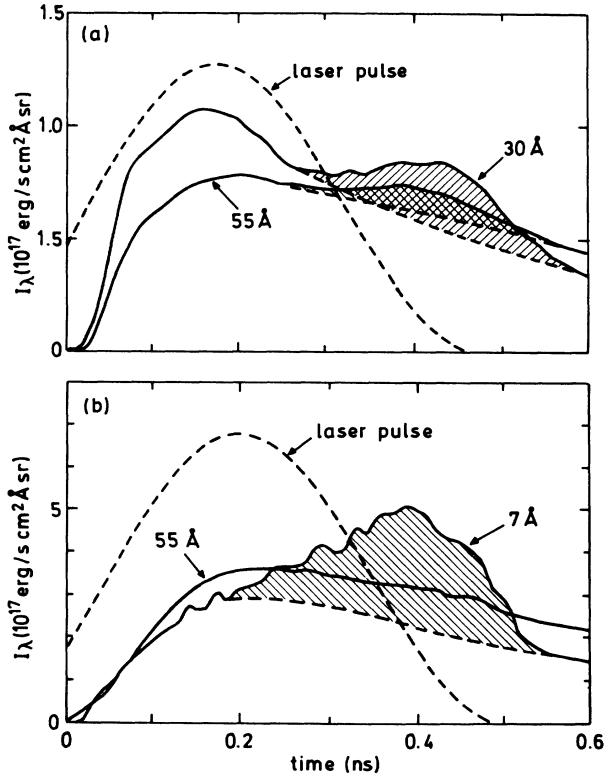

FIG. 7. The spectral intensity of the emission produced by intermediate size cavities vs time and for the indicated wavelengths. The shaded area shows schematically the contribution of the coronal plasma to the spectrum. The dashed curve indicates the laser pulse positioned so that its peak coincides with the peak of the emission in the first burst: (a) $\lambda=0.44$ μm, $D=467$ μm, traces from the spectrum shown in Fig. 3(b); (b) $\lambda=1.3$ μm, $D=456$ μm, traces from the spectrum shown in Fig. 4(b).

emission burst. The double structure of the emission is clearly visible for both wavelengths in Fig. 7(a). The excess radiation coming from the corona is indicated schematically by the shaded areas. The contribution of the corona to the overall emission diminishes for longer wavelengths. This is more pronounced in the case of cavities heated by $\lambda=1.3$-μm laser light. As can be seen from Fig. 7(b), at a 55-Å wavelength, there is no contribution from the corona to the spectral intensity. In contrast, the corona contribution dominates at wavelengths close to the N-band emission of gold (~ 5 Å).

It is evident that the corona contribution to the spectrum interferes with the temperature measurements of the indirectly heated wall elements. As explained more fully in paper I, this contribution is accounted for by subtracting it from the time-integrated spectra. The analysis of radiation confinement given in paper III is based on the corrected spectra.

D. Small cavities

The small cavities do not exhibit a double-pulse structure in their time-resolved spectra. This behavior is easily explained in terms of their size. Because the diagnostic hole is now close to the primary plasma spot, the appearance of the second burst (attributed to the coronal plasma) coincides virtually with the emission from the wall. The fact that for small cavities, the laser flux at the primary plasma spot as well as the average laser flux inside the cavity is higher, is responsible for the appearance of the M-band emission in their time-resolved spectrum, even for $\lambda=0.44$ μm [Fig. 5(a)].

From the above discussion it becomes apparent that the term "small cavity" is relative to wavelength of the laser light with which the cavity is heated. For each wavelength, there is a critical cavity diameter under which the cavity fills with plasma and the energy deposition is not localized at the rear wall of the cavity. These experiments have shown that this critical diameter is smaller for $\lambda=0.44$-μm irradiation than for $\lambda=1.3$ μm. It should be noted here that the time-integrated pinhole images from small cavities corroborate the explanation given above for the phenomena occurring in their interior (for a complete set of pinhole images for different diameter cavities see paper I, Fig. 3).

Although most of the features of the experimental observations can be explained on the basis of the coronal blow-off model, other more complicated processes can not be excluded. The spherical geometry of the cavity interior facilitates the creation of small density gradients at the beginning of the laser pulse because of the convergence of the plasma towards the center of the cavity. This creates favorable conditions for the development of parametric instabilities.[28,29] Plasma created by $\lambda=0.44$ μm is less prone to such instabilities since it is in general more collisional. However, for $\lambda=1.3$ μm, it is quite plausible that such instabilities could develop and, in some cases, lead to important redistribution of the laser energy. For example, due to instability caused disturbances in the reflecting layer, diffuse scattering of the laser light can be greatly enhanced.[30] Furthermore, the fraction of energy that is taken up by fast electrons can also increase. The observed late arrival of the second burst can then be attributed to the time that is needed for the flat density gradients to build up and for the instability to develop.[29] The choice among other processes which could produce the observed level of radiation in $\lambda=1.3$-μm experiments is difficult and ambiguous. It is obvious that a more detailed study of the hard x-ray emission from cavities is needed in order to be able to address these questions.

V. SUMMARY AND CONCLUSIONS

An overview of the results of wavelength variation experiments with laser heated cavities has been presented. The discussion in this paper is confined to temporally resolved measurements. The most important feature revealed by these measurements is the existence of a double x-ray pulse produced by intermediate size cavities heated by single-laser pulses. The double-pulse structure occurs in both cases, i.e., with $\lambda=1.3$-μm or $\lambda=0.44$-μm irradiation. The most significant difference resulting from the wavelength variation is the spectral content of the second burst in the double-pulse structure. For $\lambda=1.3$ μm, M-band emission from gold appears, while for $\lambda=0.44$-μm irradiation and comparable size cavities, M-band emission is absent.

An hypothesis has been put forward that the emission in the second burst is due to the expanding coronal plasma originating at the real wall of the cavity where the laser impinges. Within the framework of this hypothesis, most of the experimental observations for the $\lambda=0.44$-μm case are adequately explained, e.g., the delayed appearance and the spectral content of the second burst are in good agreement with the model calculations. For $\lambda=1.3$ μm, however, although the appearance of M-band emission is consistent with the hypothesis that the radiation is due to coronal plasma, the intensity observed requires that the plasma density at the center of the cavity be greater than critical. This indicates that for $\lambda=1.3$ μm, the cavity is filled with overdense plasma which prevents the laser energy from being deposited inside the cavity.

These observations provide direct experimental evidence that, in small cavities, plasma filling and entrance hole closure present a problem in coupling the laser energy to the cavity. Also, they demonstrate the qualitative improvement that ensues by changing from $\lambda=1.3$-μm to $\lambda=0.44$-μm irradiation.

ACKNOWLEDGMENTS

The authors gratefully acknowledge the help and support provided by many people throughout the progress of this work. We appreciate the assistance provided by H. Haas, P. Sachsenmaier, and V. Chevokin with the operation and characterization of the x-ray streak camera. We thank W. Fölsner for promptly providing us with well-characterized targets and H. Brändlein for her invaluable assistance with the data digitization and reduction. Without a reliable laser these experiments could not have been performed. For this we are thankful to the Asterix

III laser team, H. Baumhacker, G. Brederlow, F. Denk, A. Herrle, and G. Keller. We also thank the colleagues with whom we have discussed this work and, in particular, K. Eidmann and J. Meyer. Finally, we wish to thank S. Witkowski for his continuous support and interest in our work and for reading the manuscript and making useful suggestions. This work was supported in part by the Commission of the European Communities in the framework of the Association EURATOM–Max-Planck-Institut für Plasmaphysik.

[1]R. Sigel, Europhys. News **17**, 116 (1986); in Invited papers of the 14th European Conference on Controlled Fusion and Plasma Physics, Madrid, 1987 [Plasma Phys. Cont. Fusion **29**, 1261 (1987)].

[2]T. Mochizuki, T. Yabe, H. Azechi, K. A. Tanaka, T. Boehly, N. Miyanaga, H. Nishimura, S. Ido, M. Yamanaka, K. Nishihara, T. Norimatsu, T. Jitsuno, M. Nakatsuka, K. Mima, S. Nakai, C. Yamanaka, R. Sigel, G. D. Tsakiris, K. Eidmann, P. Herrmann, R. Pakula, P. Sachsenmaier, S. Sakabe, and S. Witkowski, in Proceedings of the Eleventh International Conference on Plasma Physics and Controlled Nuclear Fusion Research held by the International Atomic Energy Agency, Kyoto, 1986 [Nucl. Fusion Suppl. **3**, 25 (1987)].

[3]R. Pakula and R. Sigel, Z. Naturforsch. **41a**, 463 (1986).

[4]G. D. Tsakiris, P. Herrmann, R. Pakula, R. Schmalz, R. Sigel, and S. Witkowski, Europhys. Lett. **2**, 213 (1986).

[5]G. D. Tsakiris and K. Eidmann, J. Quant. Spectrosc. Radiat. Transfer **38**, 353 (1987).

[6]M. F. Rosen, D. W. Phillion, V. C. Rupert, W. C. Mead, W. L. Kruer, J. J. Thomson, H. N. Kornblum, V. W. Slivinsky, G. J. Caporaso, M. J. Boyle, and K. G. Tirsell, Phys. Fluids **22**, 2020 (1979).

[7]P. D. Rockett, W. Priedhorsky, and D. Giovanielli, Phys. Fluids **25**, 1286 (1982).

[8]W. C. Mead, E. M. Campbell, K. G. Estabrock, R. E. Turner, W. L. Kruer, P.H. Y. Lee, B. Prutt, V. C. Rupert, K. G. Tirsell, G. L. Stradling, F. Ze, C. E. Max, M. D. Rosen, and B. F. Lasinski, Phys. Fluids **26**, 2316 (1983).

[9]H. Nishimura, F. Matsuoka, M. Yagi, K. Yamada, S. Nakai, G. H. McCall, and C. Yamanaka, Phys. Fluids **26**, 1688 (1983).

[10]T. Mochizuki, T. Yabe, K. Okada, M. Hamada, N. Ikeda, S. Kiyokama, and C. Yamanaka, Phys. Rev. A **33**, 525 (1986).

[11]P. Alaterre, H. Pépin, R. Fabbro, and B. Faral, Phys. Rev. A **34**, 4184 (1986).

[12]S. R. Goldman and W. C. Mead. Nucl. Fusion **26**, 813 (1986).

[13]R. Kodama, K. Okada, N. Ikeda, M. Mineo, K. A. Tanaka, T. Mochizuki, and C. Yamanaka, J. Appl. Phys. **59**, 3050 (1986).

[14]K. Eidmann and T. Kishimoto, Appl. Phys. Lett. **49**, 377 (1986).

[15]H. N. Kornblum, R. L. Kauffman, and J. A. Smith, Rev. Sci. Instrum. **57**, 2179 (1986).

[16]P. D. Goldstone, S. R. Goldman, W. C. Mead, J. A. Cobble, G. Stradling, R. H. Day, A. Hauer, M. C. Richardson, R. S. Marjoribanks, P. A. Jaanimagi, R. L. Keck, F. J. Marshall, W. Seka, O. Barnouin, B. Yaakobi, and S. A. Letzring, Phys. Rev. Lett. **59**, 56 (1987).

[17]R. Sigel, K. Eidmann, J. Meyer-ter-Vehn, G. D. Tsakiris, and S. Witkowski, Proc. Soc. Photo-Opt. Instrum. Eng. **831**, 73 (1988).

[18]S. Sakabe, R. Sigel, G. D. Tsakiris, I. B. Földes, and P. Herrmann, preceding paper, Phys. Rev. A **38**, 5756 (1988). Also, referred to in text as paper I.

[19]R. Sigel, R. Pakula, S. Sakabe, and G. D. Tsakiris, following paper, Phys. Rev. A **38**, 5779 (1988). Also, referred to in text as paper III.

[20]I. B. Földes, R. Pakula, S. Sakabe, and R. Sigel, Appl. Phys. B **43**, 117 (1987).

[21]R. Sigel, A. G. M. Maaswinkel, and G. D. Tsakiris, in Proceedings of the 16th International Congress on High Speed Photography and Photonics, Strasbourg, 1984 [Proc. Soc. Photo-Opt. Instrum. Eng. **491**, 814 (1984)].

[22]K. Eidmann, T. Kishimoto, P. Herrmann, J. Mizui, R. Pakula, R. Sigel, and S. Witkowski, Laser Part. Beams **4**, 521 (1986).

[23]S. A. Letzring, E. I. Thorsos, W. D. Friedman, W. Seka, and J. E. Rizzo, J. Appl. Phys. **54**, 6302 (1983).

[24]K. Okada, T. Mochizuki, N. Ikeda, M. Hamada, M. Mineo, R. Kodama, and C. Yamanaka, J. Appl. Phys. **59**, 2332 (1986).

[25]P. Herrmann, R. Pakula, I. B. Földes, R. Sigel, G. D. Tsakiris, and S. Witkowski, Z. Naturforsch. **41a**, 767 (1986).

[26]D. E. Post, R. V. Jensen, C. B. Tarter, W. H. Grasberger, and W. A. Lokke, At. Data Nucl. Data Tables **20**, 397 (1977).

[27]H. R. Griem, *Plasma Spectroscopy* (McGraw-Hill, New York, 1964).

[28]H. Nishimura, H. Azechi, M. Nakai, S. Uchida, Y. Sakawa, T. Wada, H. Hasegawa, H. Sakurai, T. Yamanaka, and C. Yamanaka, Opt. Commun. **56**, 409 (1986).

[29]Y. Sakawa, K. A. Tanaka, H. Nishimura, M. Nakai, T. Yabe, H. Sakurai, Y. Izawa, Y. Kato, T. Mochizuki, M. Nakatsuka, and C. Yamanaka, Phys. Fluids **30**, 3276 (1987).

[30]K. Eidmann, G. Brederlow, R. Brodmann, R. Petsch, R. Sigel, G. Tsakiris, R. Volk, and S. Witkowski, J. Phys. D **12**, L145 (1979).

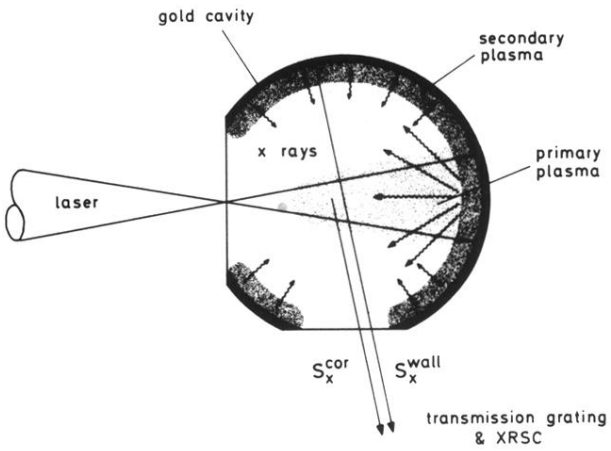

FIG. 1. Schematic drawing of the method used to heat cavities. In addition to the entrance hole through which the laser is coupled to the cavity, a diagnostic hole is used for probing the x-ray radiation generated in the cavity. The arrows indicate the line of sight of the x-ray streak camera (XRSC) which detects radiation from the secondary plasma (x-ray ablated plasma), but also from the corona of the primary plasma (laser ablated plasma).

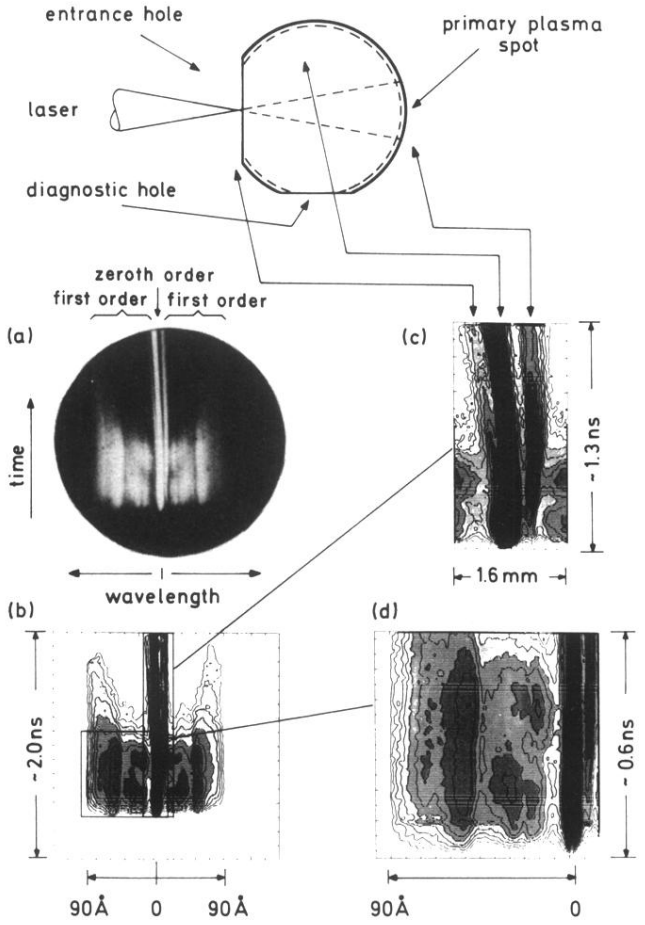

FIG. 2. Time-resolved spectrum from a cavity (laser wavelength 0.44 μm, cavity diameter 467 μm) obtained with a free-standing transmission grating and an x-ray streak camera: (a) raw data on film, (b) digitized record, (c) subframe showing the detailed structure of the zeroth order and its relation to the various emission regions of the cavity (schematic at the top), and (d) subframe used for further processing to obtain the deconvolved cavity spectrum shown in Fig. 3(b).

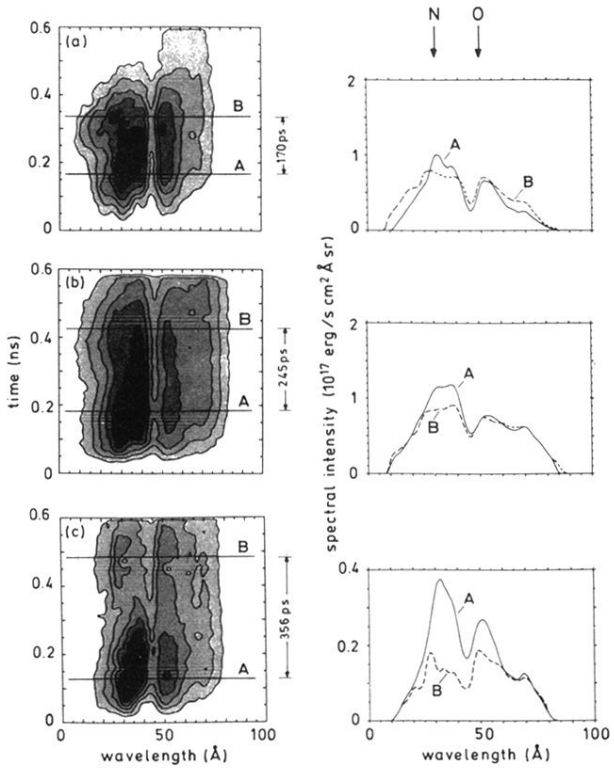

FIG. 3. Deconvolved streaked spectra from cavities irradiated with $\lambda = 0.44$-μm laser light for different cavity diameters [(a) 405 μm, (b) 467 μm, and (c) 555 μm]. The instantaneous spectra corresponding to the peak emission during the first (A) and second (B) burst are shown to the right. For each diameter, the delay Δt representing the approximate time interval between first and second burst is given.

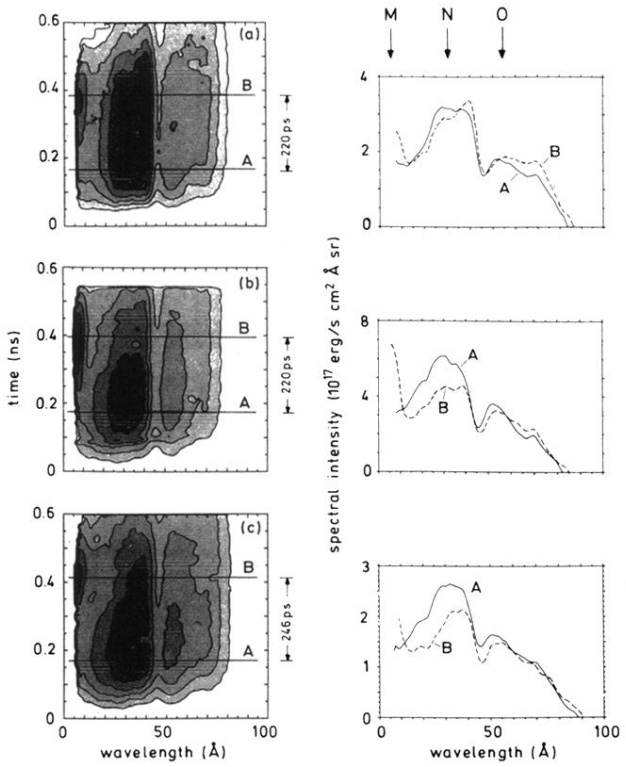

FIG. 4. Deconvolved streaked spectra from cavities irradiated with $\lambda = 1.3$-μm laser light for different cavity diameters [(a) 406 μm, (b) 456 μm, and (c) 519 μm]. The instantaneous spectra corresponding to the peak emission during the first (A) and second (B) burst are shown to the right. For each diameter, the delay Δt representing the approximate time interval between first and second burst is given. Note the appearance of the M-band emission during the second burst.

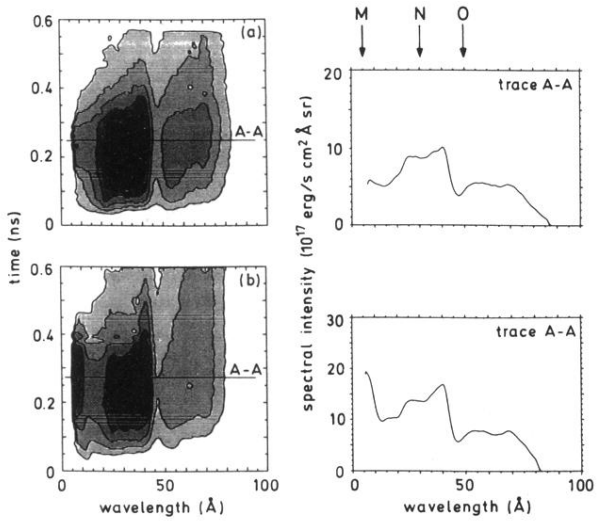

FIG. 5. Deconvolved streaked spectra produced by small cavities ($D=252$ μm) for (a) $\lambda=0.44$-μm and (b) $\lambda=1.3$-μm irradiation. The instantaneous spectrum corresponding approximately to peak emission (trace A-A) for the two cases is also shown.